Thioxanthone-containing blue thermally activated delayed fluorescent emitter

Natsuko Kanno, Yongxia Ren, Yu Kusakabe, Katsuaki Suzuki, Katsuyuki Shizu, Hiroyuki Tanaka, Yoshimasa Wada, Hiromichi Nakagawa, Jan Geldsetzer, and Hironori Kaji*

Institute for Chemical Research, Kyoto University, Uji, Kyoto, 611-0011, Japan

E-mail: kaji@scl.kyoto-u.ac.jp

Accelerating reverse intersystem crossing (RISC) without sacrificing fast radiative decay is effective in suppressing efficiency roll-off (eRO) in thermally activated delayed fluorescence (TADF)-based organic light-emitting diodes. We here report a TADF emitter, CC-TXO-I, combining a bicarbazole donor (CC) and a sulfur-containing acceptor (TXO). The CC is used to accelerate radiative decay via moderate donor-acceptor torsion angle, and the TXO is expected to provide fast RISC by the heavy atom effect. We realized very large rate constants of RISC (k_{RISC}) of ~10^7 s^{-1}. Both k_{RISC} and rate constants of radiative decay of CC‐TXO‐I as increased doping concentration, attributing improved eROs.

Organic light-emitting diodes (OLEDs) have several attractive characteristics such as high luminous efficiency, low power consumption, high color contrast, light weight, flexibility, and eco-friendliness.[1–5] To further improve the efficiency of noble-metal-free OLEDs, thermally activated delayed fluorescence (TADF) emitters have been actively investigated as new-generation luminescent materials.[6–8] Conventional fluorescent emitters can convert only singlet excitons into light, resulting in low internal quantum efficiency (IQE) of 25% at the maximum owing to spin statics.[9] In contrast, TADF emitters can achieve IQE of 100% because they can convert not only singlet excitons but also triplet excitons into light via a reverse intersystem crossing (RISC) process from a triplet state (T_n, typically T_1) to an excited singlet state (S_m, typically S_1) (n and m are natural numbers with ≥ 1).[6] Actually, some TADF emitters showed an IQE of ≈100%.[10–12]

Nevertheless, TADF-based OLEDs have a serious problem of efficiency roll-off (eRO) in the high luminance region.[9,13] This is because triplet excitons generated on TADF emitters have relatively long lifetimes, which allow the quench processes such as triplet-triplet annihilation (TTA) and singlet-triplet annihilation (STA).[14,15] Therefore, shortening an exciton lifetime can be an effective approach to reduce an exciton density in the emitting layer and then suppress eRO. A short exciton lifetime can be realized by fast RISC and fast radiative decay processes. When the transition between the highest occupied molecular orbital (HOMO) and the lowest unoccupied molecular orbital (LUMO) mainly contributes to the electronic configuration of S_1, a large spatial overlap between the HOMO and LUMO leads to the large rate constant of radiative decay (k_r).[16,17] Besides, according to Fermi's golden rule, a rate constant of RISC (k_{RISC}) can be expressed as[18]

$$k_{RISC} \propto \left|\langle S|\hat{H}_{SOC}|T\rangle\right|^2 exp\left(\frac{-\Delta E_{ST}}{k_B T}\right) \qquad (1)$$

where $\left|\langle S|\hat{H}_{SOC}|T\rangle\right|$, ΔE_{ST}, k_B, and T are the spin-orbit coupling matrix element values (SOCMEVs), the energy gap between S_1 and T_1, the Boltzmann constant, and temperature, respectively. This equation indicates that large SOCMEVs and small ΔE_{ST} are effective for fast RISC. Small ΔE_{ST} can be realized by a small spatial HOMO-LUMO overlap and it is challenging to reconcile the large k_{RISC} and large k_r from the perspective of a HOMO-LUMO overlap.[19]

In this study, we designed a TADF emitter by combining a bicarbazole donor and sulfur-containing acceptor, aiming to achieve an emitter with both large k_{RISC} and large k_r

simultaneously. Since the heavy atom effect is expected to increase SOCMEVs, TADF emitters have been designed containing non-metal heavy atoms, such as sulfur[20–23], selenium[24–26], and halogens[27–29]. Among them, thioxanthone (TXO)-based emitters are especially noteworthy in terms of fast RISC.[21,22] For instance, MCz-TXO, reported by us,[22] exhibited a very large k_{RISC} of ~ 2×10^8 s^{-1}. MCz-TXT, reported by Yasuda *et al.*[21], similarly showed the large k_{RISC} of 1.1×10^8 s^{-1}. Therefore, TXO was selected as the acceptor in this work to realize large k_{RISC}.

Additionally, a moderate torsion angle between donor and acceptor is preferable to enlarge a HOMO-LUMO overlap and therefore k_r.[30] In one example, CCX-I (Fig. S2), which was reported by us,[31] containing 9*H*-3,9'-bicarbazole (CC) as a donor was determined to have a moderate torsion angle of 50° by the quantum chemical calculations because the carbazole unit contained in CC shows a relatively small steric hindrance. As a result, CCX-I was calculated to have a sizable oscillator strength between S_1 and ground state (S_0), and experimentally exhibited the very large k_r of 5.9×10^7 s^{-1}. On the basis of this report, we chose the CC as a donor.

On the basis of the above fact, a donor-acceptor type TADF emitter, 3-(9*H*-[3,9'-bicarbazol]-9-yl)-9*H*-thioxanthen-9-one (CC-TXO-I) [Fig. 1(a)], was designed. Quantum chemical calculations based on density functional theory (DFT) and time-dependent DFT with Tamm-Dancoff approximation were performed using the Amsterdam Density Functional program package (ADF2019.302).[32] With triple zeta basis set and PBE0 functional, the geometry optimization of the ground state, excitation energies, as well as the highest occupied natural transition orbital (HONTO) and lowest unoccupied natural transition orbital (LUNTO) of S_1 and T_n (where n = 1, 2), together with SOCMEVs between S_1 and T_n were calculated. The calculation results are shown in Fig. 1 and Table I. Table I also contains the results for CCX-I, which has a similar chemical structure to CC-TXO-I but the acceptor contains oxygen, not sulfur. The S_1 energy of CC-TXO-I was calculated to be 3.07 eV, which is similar to that of the blue emitter, CCX-I (3.10 eV), predicting CC-TXO-I showed blue emission. As shown in Fig. 1(a), the torsion angle between CC and TXO is 60°. The HOMO and LUMO distributions are mostly spatially separated, but slightly overlapped as shown in Fig. 1(b). Besides, CC-TXO-I was calculated to possess relatively small ΔE_{ST} of 0.17 eV and the large oscillator strength of 0.1003, indicating that its torsion

angle is suitable for the simultaneous realization of a large k_{RISC} and large k_r. Moreover, the oscillator strength of CC-TXO-I is close to that of CCX-I (0.1050), evidencing that CC-TXO-I may show the large k_r as we designed (k_r of CCX-I is 8.7×10^7 s^{-1} in the doped film). Fig. 1(d) shows natural transition orbital (NTO) results for CC-TXO-I. The S_1 was attributed to a charger transfer (CT) characteristic, while T_1 and T_2 were assigned to hybridized local and charge transfer (HLCT) characteristics. In addition to this, large orbital coefficients were observed over the sulfur atom in HONTO of T_1 and T_2. As a result, notable SOCMEVs of 1.69, 2.01 cm^{-1} were calculated for $T_1 \rightarrow S_1$ and $T_2 \rightarrow S_1$ transition, respectively (Table I). Compared to SOCMEVs of CCX-I, the enhanced SOC of CC-TXO-I can be attributed to the heavy atom effect resulting from sulfur. A similar effect has been found in previous studies.[24,25] From these calculations, CC-TXO-I are expected to exhibit blue emission with large k_{RISC} and k_r.

Prior to photophysical characterizations, CC-TXO-I was synthesized and train sublimated (see detail in Supplementary Information). Fig. 2 shows the fluorescence, phosphorescence, and UV-vis absorption spectra for 1×10^{-4} M CC-TXO-I in an oxygen-free toluene. In the UV-vis absorption spectrum, absorptions of CC and TXO are observed in the region of 300–350 nm[33] and 350–380 nm[34], respectively. Also, the absorption in the region around 400 nm could be assigned to intramolecular CT absorption. In addition, the HOMO-LUMO gap of CC-TXO-I was determined to be 3.09 eV from the onset of the absorption spectra (the calculated value is 3.07 eV), resulting in blue emission with the emission peak maximum wavelength (λ_{MAX}) of 454 nm and CIE (x, y) = (0.17, 0.18) in fluorescence spectra. From the onset of both fluorescence and phosphorescence spectra, the experimental ΔE_{ST} was determined to be 0.19 eV, which agreed well with calculated ΔE_{ST} of 0.17 eV.

We prepared several CC-TXO-I doped films with different host materials and conducted photophysical measurements. As shown in Table SI, we found that 2,8-bis(diphenylphosphineoxide)dibenzofuran (PPF) was an appropriate host for CC-TXO-I in terms of the photoluminescence (PL) quantum yield (Φ_{PL}). Table SII summarizes the doping concentration dependence of λ_{MAX} and Φ_{PL}s for vacuum-processed CC-TXO-I:PPF doped films. 6, 15, and 20 vol% CC-TXO-I:PPF exhibited similar Φ_{PL} of 84, 83, and 84%, respectively, while the PL spectra were red-shifted with increasing the concentration, probably due to the polarity of CC-TXO-I itself. Fig. S5(a) exhibits the transient PL decays

of CC-TXO-I:PPF doped films at each doping concentration. All three concentrations of CC-TXO-I showed clear delayed emission of microsecond order, indicating TADF characteristics. The rate constants of CC-TXO-I:PPF doped film were determined with the equation reported in Ref. 34 and summarized in Table II. Owing to the heavy atom effect of sulfur in TXO, CC-TXO-I exhibited fast RISC with the k_{RISC} of ~10^7 s^{-1} as we designed, which is three orders of magnitude larger than that of the CCX-I doped film (2.3×10^4 s^{-1}). In contrast, CC-TXO-I doped films showed k_r of ~10^6 s^{-1}. In comparison with the k_r of the CCX-I doped film at the same doping concentration (5.9×10^7 s^{-1}), that of CC-TXO-I was not large as expected from the calculation results, although the relatively high Φ_{PL} of 84%. Additionally, we performed temperature-dependent transient PL decay measurement for 6 vol% CC-TXO-I:PPF doped film. As shown in Fig. S6, the delayed component was increased with temperature increasing. This result confirmed that CC-TXO-I possessed TADF property.

Finally, we fabricated OLEDs using CC-TXO-I-doped films as emitting layers by vacuum deposition. The device structure is as follows: ITO (50 nm)/4,4′-cyclohexylidenebis[*N*,*N*-bis(4-methylphenyl)benzenamine] (TAPC) (60 nm)/1,3-bis(9,9-dimethylacridin-10(9*H*)-yl)benzene (mAP) (10 nm)/*X* vol% CC-TXO-I (*X* = 6, 15, 21) : PPF(40 nm)/PPF (10 nm)/1,3-bis[3,5-di(pyridin-3-yl)phenyl]benzene (BmPyPhB)[35] (35 nm)/lithium quinolin-8-olate (Liq) (1 nm)/Al (80 nm) as shown in Fig. 3(a). TAPC and BmPyPhB were used as a hole transport layer and an electron transport layer, respectively. mAP and PPF layers were inserted to block electrons and holes, respectively. Fig. 3(b), 3(c), and 3(d) show external quantum efficiency (EQE)-luminance characteristics, electroluminescence (EL) spectra, and current density-voltage-luminance characteristics, respectively. The EL properties were summarized in Table III. CC-TXO-I-based OLEDs showed blue to greenish blue emission with maximum EQEs (EQE_{max}s) of 19.0, 17.7, and 17.2% for 6, 15, and 21 vol%, respectively. Among them, 21 vol% device showed the smallest eRO; EQEs at 100 and 1000 cd m^{-2} (EQE_{100} and EQE_{1000}, respectively) were 15.3% and 13.1%; this means the EQE_{100} and EQE_{1000} dropped by 11.0% and 23.8% relative to its EQE_{max}, respectively. Although CC-TXO-I showed the very large k_{RISC} of ~10^7 s^{-1}, eRO was still observed. The reason can be attributed to the relatively large delayed lifetime (τ_d) in the CC-TXO-I doped films, inducing TTA and STA in the high luminance region. In fact, the

larger the τ_d, the greater eRO (see Table II and Fig. 3; 6 vol% device exhibited the largest eRO). In CC-TXO-I's case, the large imbalance between k_r (~10^6 s^{-1}) and k_{ISC} (~10^9 s^{-1}) is considered to be bottlenecks in achieving eRO-free OLEDs.

In conclusion, we have developed a blue TADF emitter, CC-TXO-I, by combining CC as a donor and TXO as an acceptor. TXO was selected to enhance RISC due to the heavy atom effect of sulfur and CC was selected to achieve a moderate HOMO-LUMO overlap. The quantum chemical calculations indicated that CC-TXO-I had large SOCMEVs of 1.69 cm^{-1} between S_1 and T_1, and 2.01 cm^{-1} between S_1 and T_2. The doped films using CC-TXO-I as a dopant showed the TADF properties of the k_{RISC} of ~10^7 s^{-1}, k_r of ~10^6 s^{-1}, and the Φ_{PL} of 84%. The EQE_{max} of 19.0%, and the maximum luminance of 17,200 cd m^{-2} were obtained for CC-TXO-I-based OLEDs at doping concentrations of 6 and 21 vol%, respectively. Both k_{RISC} and k_r increased with the doping concentration, attributing suppressed eROs, and this result suggests that accelerated RISC, and radiative decay effectively realize OLEDs with reduced eROs.

Acknowledgments

This work was supported by JSPS KAKENHI Grant Numbers JP20H05840 (Grant-in-Aid for Transformative Research Areas, "Dynamic Exciton"), JP17H01231, JSPS Core-to-Core Program, and Kyulux, Inc. Computation time was provided by the Super Computer System, Institute for Chemical Research, Kyoto University. Nuclear magnetic resonance measurements and mass spectrometry measurements were supported by the international Joint Usage/Research Centre (iJURC) at the Institute for Chemical Research, Kyoto University.

References

1) C. W. Tang and S. A. VanSlyke, Appl. Phys. Lett. **51**, 913 (1987).
2) B. Geffroy, P. le Roy and C. Prat, Polym. Int. **55**, 572 (2006).
3) S. J. Zou, Y. Shen, F. M. Xie, J. De Chen, Y. Q. Li and J. X. Tang, Mater. Chem. Front. **4**, 788 (2020).
4) Y. Huang, E. L. Hsiang, M. Y. Deng and S. T. Wu, Light Sci. Appl. **9**, 105 (2020).
5) G. Hong, X. Gan, C. Leonhardt, Z. Zhang, J. Seibert, J. M. Busch and S. Bräse, Adv. Mater. **33**, 2005630 (2021).
6) H. Uoyama, K. Goushi, K. Shizu, H. Nomura and C. Adachi, Nature **492**, 234 (2012).
7) Z. Yang, Z. Mao, Z. Xie, Y. Zhang, S. Liu, J. Zhao, J. Xu, Z. Chi and M. P. Aldred, Chem. Soc. Rev. **46**, 915 (2017).
8) H. Nakanotani, Y. Tsuchiya and C. Adachi, Chem. Lett. **50**, 938 (2021).
9) C. Murawski, K. Leo and M. C. Gather, Adv. Mater. **25**, 6801 (2013).
10) J. W. Sun, J. H. Lee, C. K. Moon, K. H. Kim, H. Shin and J. J. Kim, Adv. Mater. **26**, 5684 (2014).
11) H. Kaji, H. Suzuki, T. Fukushima, K. Shizu, K. Suzuki, S. Kubo, T. Komino, H. Oiwa, F. Suzuki, A. Wakamiya, Y. Murata and C. Adachi, Nat. Commun. **6**, 8476 (2015).
12) D. R. Lee, M. Kim, S. K. Jeon, S. H. Hwang, C. W. Lee and J. Y. Lee, Adv. Mater. **27**, 5861 (2015).
13) M. Inoue, T. Serevičius, H. Nakanotani, K. Yoshida, T. Matsushima, S. Juršenas and C. Adachi, Chem. Phys. Lett. **644**, 62 (2016).
14) K. Masui, H. Nakanotani and C. Adachi, Org. Electron. **14**, 2721 (2013).
15) A. Niwa, S. Haseyama, T. Kobayashi, T. Nagase, K. Goushi, C. Adachi and H. Naito, Appl. Phys. Lett. **113**, 083301 (2018).
16) K. Shizu, T. Miwa, Y. Wada, I. Ogata and H. Kaji, J Photopolym. Sci. Technol. **30**, 475 (2017).
17) X. K. Chen, Y. Tsuchiya, Y. Ishikawa, C. Zhong, C. Adachi and J. L. Brédas, Adv. Mater. **29**, 1702767 (2017).
18) J. U. Kim, I. S. Park, C. Y. Chan, M. Tanaka, Y. Tsuchiya, H. Nakanotani and C.

Adachi, Nat. Commun. **11**, 1765 (2020).

19) R. Gómez-Bombarelli, J. Aguilera-Iparraguirre, T. D. Hirzel, D. Duvenaud, D. Maclaurin, M. A. Blood-Forsythe, H. S. Chae, M. Einzinger, D. G. Ha, T. Wu, G. Markopoulos, S. Jeon, H. Kang, H. Miyazaki, M. Numata, S. Kim, W. Huang, S. I. Hong, M. Baldo, R. P. Adams and A. Aspuru-Guzik, Nat. Mater. **15**, 1120 (2016).

20) I. S. Park, K. Matsuo, N. Aizawa and T. Yasuda, Adv. Funct. Mater. **28**, 1802031 (2018).

21) N. Aizawa, A. Matsumoto and T. Yasuda, Sci. Adv. **7**, eabe5769 (2021).

22) Y. Ren, Y. Wada, K. Suzuki, Y. Kusakabe, J. Geldsetzer and H. Kaji, Appl. Phys. Express **14**, 071003 (2021).

23) M. Cai, M. Auffray, D. Zhang, Y. Zhang, R. Nagata, Z. Lin, X. Tang, C. Y. Chan, Y. T. Lee, T. Huang, X. Song, Y. Tsuchiya, C. Adachi and L. Duan, Chem. Eng. J. **420**, 127591 (2021).

24) B. H. Drummond, G. C. Hoover, A. J. Gillett, N. Aizawa, W. K. Myers, B. T. McAllister, S. T. E. Jones, Y. J. Pu, D. Credgington and D. S. Seferos, J. Phys. Chem. C **124**, 6364 (2020).

25) S. Goto, Y. Nitta, N. O. Decarli, L. E. de Sousa, P. Stachelek, N. Tohnai, S. Minakata, P. de Silva, P. Data and Y. Takeda, J. Mater. Chem. C **9**, 13942 (2021).

26) P. Sharif, E. Alemdar, S. Ozturk, O. Caylan, T. Haciefendioglu, G. Buke, M. Aydemir, A. Danos, A. P. Monkman, E. Yildirim, G. Gunbas, A. Cirpan and A. Oral, Adv. Funct. Mater. 2207324 (2022).

27) Y. Xiang, Y. Zhao, N. Xu, S. Gong, F. Ni, K. Wu, J. Luo, G. Xie, Z. H. Lu and C. Yang, J. Mater. Chem. C **5**, 12204 (2017).

28) S. Gan, S. Hu, X. L. Li, J. Zeng, D. Zhang, T. Huang, W. Luo, Z. Zhao, L. Duan, S. J. Su and B. Z. Tang, ACS Appl. Mater. Interfaces **10**, 17327 (2018).

29) H. S. Kim, J. Y. Lee, S. Shin, W. Jeong, S. H. Lee, S. Kim, J. Lee, M. C. Suh and S. Yoo, Adv. Funct. Mater. **31**, 2104646 (2021).

30) T. T. Bui, F. Goubard, M. Ibrahim-Ouali, D. Gigmes and F. Dumur, Appl. Sci. **8**, 494 (2018).

31) T. Miwa, S. Kubo, K. Shizu, T. Komino, C. Adachi and H. Kaji, Sci. Rep. **7**, 284 (2017).

32) G. Te Velde, F. M. Bickelhaupt, E. J. Baerends, C. Fonseca Guerra, S. J. A. Van Gisbergen, J. G. Snijders and T. Ziegler, J. Comput. Chem. **22**, 931 (2001).

33) M. Belletête, M. Bédard, M. Leclerc and G. Durocher, J. Mol. Struct. **679**, 9 (2004).

34) T. Chi, P. Somers, D. A. Wilcox, A. J. Schuman, V. Iyer, R. Le, J. Gengler, M. Ferdinandus, C. Liebig, L. Pan, X. Xu and B. W. Boudouris, J. Polym. Sci. Part B Polym. Phys. **57**, 1462 (2019).

35) H. Sasabe, E. Gonmori, T. Chiba, Y. J. Li, D. Tanaka, S. J. Su, T. Takeda, Y. J. Pu, K. I. Nakayama and J. Kido, Chem. Mater. **20**, 5951 (2008).

Figure Captions

Fig. 1. Calculation results for CC-TXO-I. (a) Chemical structure and torsion angle. (b) HOMO-LUMO distributions and energies. (c) Energy diagram. (d) HONTO-LUNTO distributions of S_1 and T_n (n = 1, 2).

Fig. 2. UV-vis absorption (dash line), fluorescence (solid line), and phosphorescence (dash-dot line) spectra of CC-TXO-I in oxygen-free toluene solution at a concentration of 1×10^{-4} M. The phosphorescence spectrum was measured at 77 K and emission spectra were excited at 380 nm. A photograph of PL emission in the solution and its CIE coordinates are also shown in the figure.

Fig. 3. EL performances of CC-TXO-I-based OLEDs. (a) Device structure (X = 6, 15, or 21). (b) EQE-luminance characteristics. (c) EL spectra at 100 cd m^{-2} with photographs of OLEDs. (d) Current density-voltage-luminance characteristics.

Table I. Calculated electronic properties for CC-TXO-I and CCX-I.

Molecules	S_1 (eV)[a]	f[b]	SOCMEV (cm^{-1}) / $\Delta E_{S1\text{-}Tn}$ (eV)[c]	
			T_1	T_2
CC-TXO-I	3.07	0.1003	1.69 / 0.17	2.01 / 0.06
CCX-I[31]	3.10	0.1050	0.32 / 0.13	0.75 / −0.20

a) The S_0-S_1 excitation energy. b) Oscillator strength for the $S_0 \rightarrow S_1$ transition. c) The SOCMEVs and the energy difference between S_1 and T_n (n = 1, 2).

Table II. Lifetimes and rate constants of X vol% CC-TXO-I:PPF doped films.

X (vol%)	τ_p[a] (ns)	τ_d[a] (μs)	k_r[b] (10^6 s^{-1})	k_{nr}^s[b] (10^5 s^{-1})	k_{ISC}[b] (10^9 s^{-1})	k_{RISC}[b] (10^7 s^{-1})
6	0.8	31.8	1.6	3.0	13	2.1
15	1.3	13.9	1.8	3.5	7.4	2.5
20	1.6	8.7	2.0	3.8	6.0	3.1

a) Prompt lifetime (τ_p) and delayed lifetime (τ_d). b) Rate constants of radiative decay (k_r), nonradiative decay from S_1 (k_{nr}^s), intersystem crossing process (k_{ISC}), and reverse intersystem crossing process (k_{RISC}).

Table III. Performances of OLEDs using X vol% CC-TXO-I:PPF.

X (vol%)	CIE(x, y)[a]	EQE_{max}[b] (%)	EQE_{100} / EQE_{1000}[c] (%)	Roll-off$_{100}$ / Roll-off$_{1000}$[d] (%)	L_{max}[e] (cd m^{-2})
6	(0.17, 0.28)	19.0	15.3 / 10.3	19.5 / 45.8	7,592
15	(0.19, 0.36)	17.7	16.9 / 13.9	4.5 / 21.5	12,190
21	(0.20, 0.38)	17.2	15.3 / 13.1	11.0 / 23.8	17,200

a) CIE coordinates at 100 cd m^{-2}. b) Maximum EQE. c) EQE_Y means EQE at Y cd m^{-2}. d) Roll-off$_Y$ = (EQE_{max} − EQE_Y) / EQE_{max}. e) Maximum luminance.

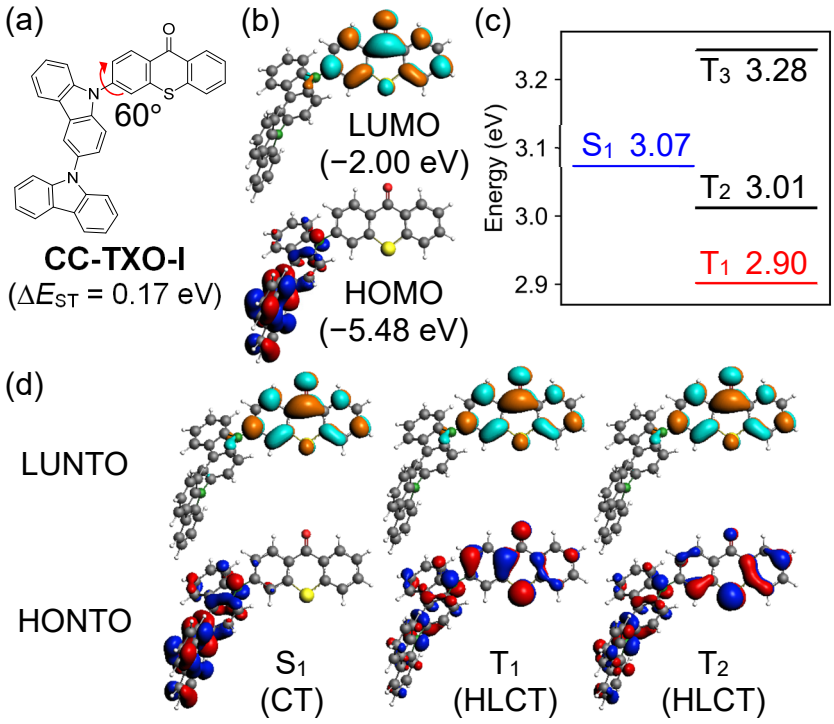
(a)
60°
CC-TXO-I
(ΔEST = 0.17 eV)
(b)
LUMO
(−2.00 eV)
HOMO
(−5.48 eV)
(c)
Energy (eV)
3.2
3.1
3.0
2.9
T3 3.28
S1 3.07
T2 3.01
T1 2.90
(d)
LUNTO
HONTO
S1
(CT)
T1
(HLCT)
T2
(HLCT)

Fig.1.

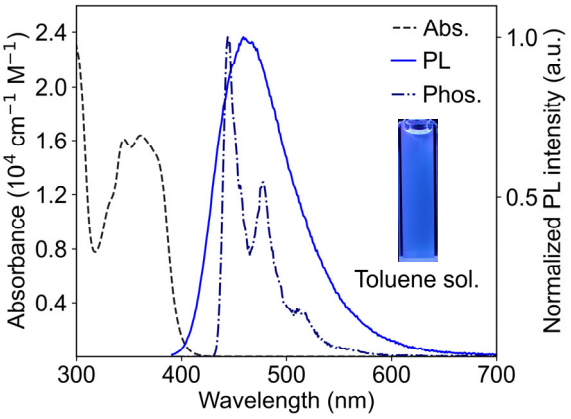
Absorbance (10^4 cm^−1 M^−1)
2.4
2.0
1.6
1.2
0.8
0.4
300
400
500
600
700
Wavelength (nm)
Abs.
PL
Phos.
Toluene sol.
1.0
0.5
Normalized PL intensity (a.u.)

Fig. 2.

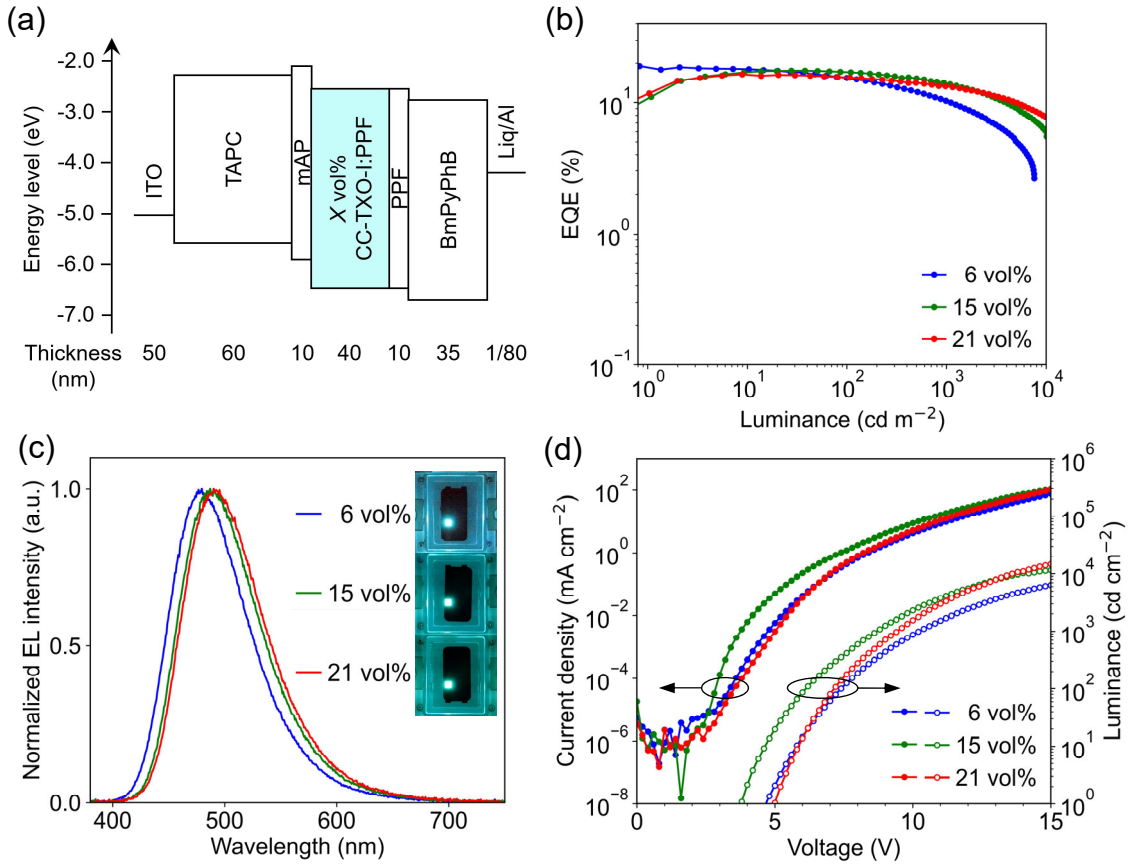
(a)
Energy level (eV)
-2.0
-3.0
-4.0
-5.0
-6.0
-7.0
ITO
TAPC
mAP
X vol%
CC-TXO-I:PPF
PPF
BmPyPhB
Liq/Al
Thickness (nm)
50
60
10
40
10
35
1/80
(b)
EQE (%)
Luminance (cd m−2)
6 vol%
15 vol%
21 vol%
(c)
Normalized EL intensity (a.u.)
Wavelength (nm)
6 vol%
15 vol%
21 vol%
(d)
Current density (mA cm−2)
Luminance (cd cm−2)
Voltage (V)
6 vol%
15 vol%
21 vol%

Fig. 3.

Supplementary information for:

Thioxanthone-containing blue thermally activated delayed fluorescent emitter

Natsuko Kanno, Yongxia Ren, Yu Kusakabe, Katsuaki Suzuki, Katsuyuki Shizu, Hiroyuki Tanaka, Yoshimasa Wada, Hiromichi Nakagawa, Jan Geldsetzer, and Hironori Kaji*

Institute for Chemical Research, Kyoto University, Uji, Kyoto, 611-0011, Japan
E-mail: kaji@scl.kyoto-u.ac.jp

1. Synthesis and characterization

1.1. Procedure for material characterization

^{1}H and ^{13}C NMR spectra were obtained with JEOL ECA (600 MHz for ^{1}H and 151 MHz for ^{13}C). $CDCl_3$ was used as a deuterated solvent and all measurements were performed at 300 K. Chemical shifts are reported in δ ppm, using tetramethylsilane for ^{1}H NMR and solvent peaks for ^{13}C NMR spectra as internal standards. Atmospheric pressure chemical ionization (APCI) mass spectra were measured with a Bruker micrOTOF-Q II (Bruker, Germany).

1.2. Synthesis procedure

1.2.1. Synthesis of compound **S1**

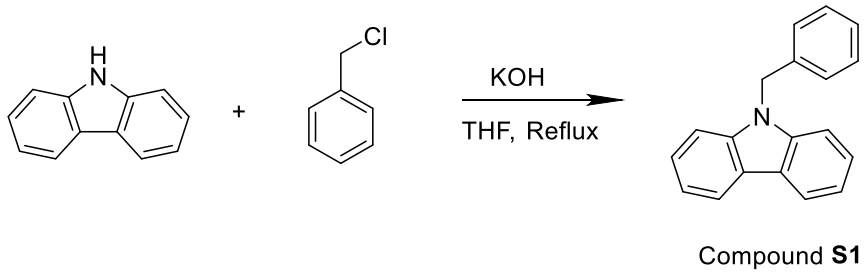

Supplementary Scheme 1. Synthesis of compound **S1**.

Carbazole (25.1 g, 150 mmol, 1 eq) and potassium hydroxide (41.0 g, 730 mmol, 4.2 eq) were placed in a two-necked flask equipped with a magnetic stirrer and a reflux condenser. The flask was evacuated and backfilled with argon. Then, 250 mL of THF was added to the mixture followed by the addition of benzyl chloride (57.0 g, 450 mmol, 3 eq). The reaction mixture was heated to reflux for 66 h. After cooling to room temperature, the suspension was poured into water, extracted three times with dichloromethane. The combined organic phase washed sequentially with a saturated ammonium chloride solution, water and brine. After drying over Na_2SO_4, the solvent was removed under reduced pressure and the crude product was recrystallized from ethanol to give white needles (compound **S1**, 35.3 g, 137 mmol, 92%). The crystals were thoroughly washed with hexane to remove excess benzyl chloride which would interfere with the subsequent bromination reactions. The analytical data matched Ref. S1.

1.2.2. Synthesis of compound **S2**

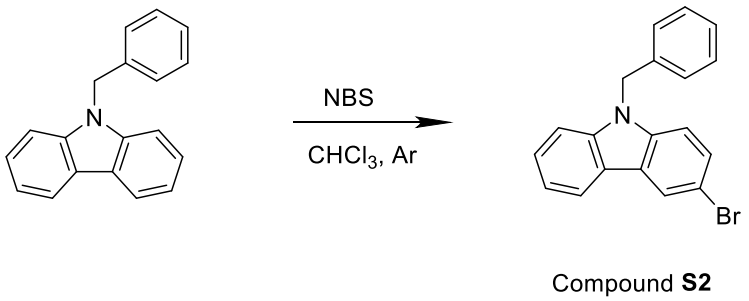

Supplementary Scheme 2. Synthesis of compound **S2**.

N-benzylcarbazole (Compound **S1**, 10.3 g, 40 mmol, 1 eq) and *N*-bromosuccinimide (NBS) (4.84 g, 41 mmol, 1.025 eq) were dissolved in 200 mL of chloroform. The flask was flushed with argon and stirred in the dark at 30 °C for 3 h. The crude reaction mixture was washed sequentially with a sodium thiosulfate solution, water and brine. The organic phase was dried over Na_2SO_4 and the solvent was removed under reduced pressure. The crude product was recrystallized from ethanol yielding 10.8 g of white needles which were found to be 70% of desired product and 30% of recovered starting material by NMR analysis (27.9 mmol isolated product, 70% yield, compound **S2**). As unbrominated, protected carbazole was deemed inconsequential to the following cross-coupling reactions, the reaction product was not purified further. The analytical data matched Ref S2.

1.2.3. Synthesis of compound **S3**

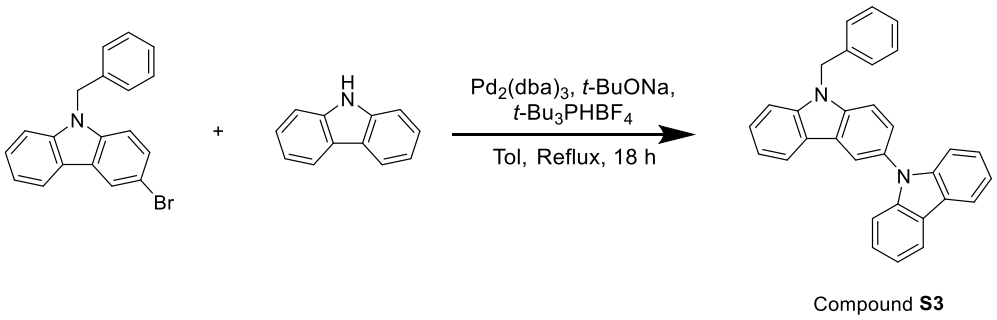

Supplementary Scheme 3. Synthesis of compound **S3**.

N-benzyl-3-bromocarbazole (Compound **S2**, 1.68 g, 5 mmol, 1 eq), carbazole (836 mg, 5

mmol, 1 eq), sodium *tert*-butoxide (*t*-BuONa, 961 mg, 10 mmol, 2 eq), tris(dibenzylideneacetone) dipalladium ($Pd_2(dba)_3$, 137 mg, 150 µmol, 3 mol-%) and tri-*tert*-butylphosphonium tetrafluoroborate (*t*-Bu_3PHBF_4, 87 mg, 300 µmol, 6 mol-%) were added to a Schlenk flask equipped with a magnetic stirrer. The flask was evacuated and backfilled with argon. After adding 50 mL of dry toluene, the flask was sealed and heated to 125 °C for 18 h. The reaction mixture was allowed to cool to room temperature before being filtrated through celite and washed down with ethyl acetate. The crude product was purified by column chromatography (hexane:ethyl acetate =15:1) and the coupling product (Compound **S3**, 1.75g, 4.13 mmol, 83%) was isolated as a white powder. The analytical data matched Ref S3.

1.2.4. Synthesis of compound **S4**

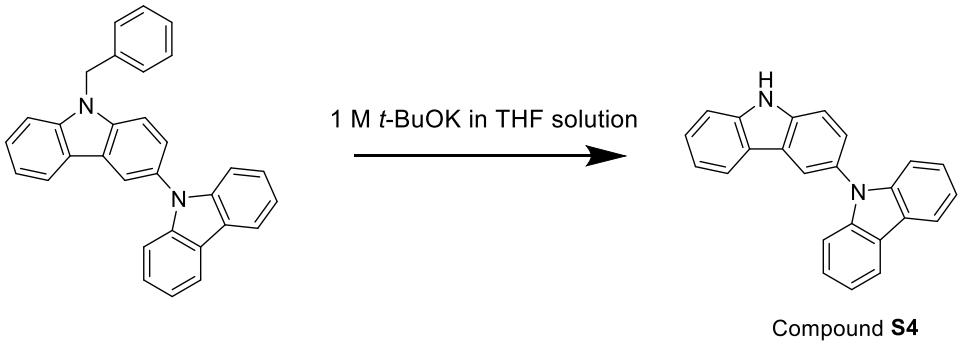

Supplementary Scheme 4. Synthesis of compound **S4**.

Benzyl-protected carbazolylcarbazole (Compound **S3**, 1.94 g, 4.58 mmol, 1 eq) were dissolved in 143 mL of DMSO in a two-necked flask equipped with a magnetic stirrer. 45.8 mL freshly prepared 1 M of potassium *tert*-Butoxide solution (5.61 g in 50 mL dry THF) was added rapidly under stirring. After 10 min, air was bubbled through the solution, which was closely monitored to prevent spillage as stable bubbles tended to develop at various times. After 3 h, bubbling was terminated and the solution poured into 200 mL of water to which about 1 g of NaCl had been added; this suspension was stirred for approximately 1 h. Thereafter, the top of the beaker was covered with aluminium foil and the suspension allowed to rest in the fridge over 3 nights. The precipitate was collected by filtration and dried in vacuum. The desired product (Compound **S4**, 1.51 g, 4.54 mmol) were isolated as a

white powder and shown to require no further purification. The analytical data matched Ref S3.

1.2.5. Synthesis of compound **CC-TXO-I**

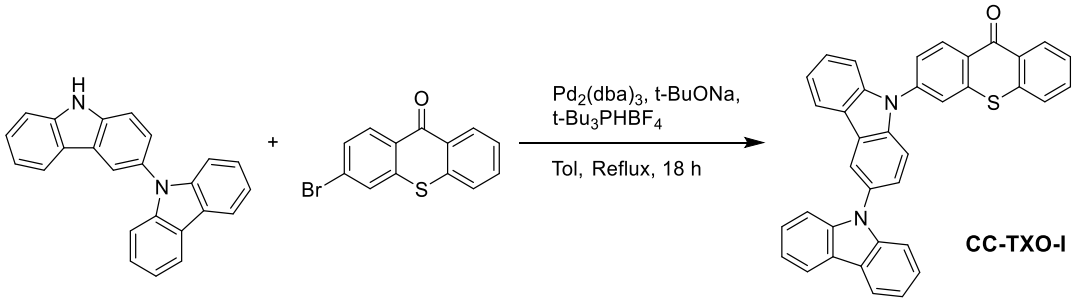

Supplementary Scheme 5. Synthesis of **CC-TXO-I**.

3-carbazolyl-carbazole (Compound **S4**, 665 mg, 2 mmol, 1 eq), 3-bromothioxanthone (582 mg, 2 mmol, 1 eq), sodium *tert*-butoxide (*t*-BuONa, 384 mg, 4 mmol, 2 eq), tris(dibenzylideneacetone)dipalladium ($Pd_2(dba)_3$, 91.6 mg, 100 µmol, 5 mol-%) and tri-*tert*-butylphosphonium tetrafluoroborate (*t*-Bu_3PHBF_4, 58.0 mg, 200 µmol, 10 mol-%) were added to a Schlenk flask equipped with a magnetic stirrer. The flask was evacuated and backfilled with argon three times and 20 mL of dry toluene were added. The flask was sealed and heated to reflux for 18 h. During this time, a yellow precipitate began gathering on the walls of the flask. After cooling to room temperature, the crude reaction mixture was filtrated through celite, washed with excess dichloromethane until the filtrate no longer fluoresced under 360 nm UV light. The product was purified by column chromatography (hexane:DCM =1:1) and subsequent recrystallization from chloroform/hexane. Bright yellow crystals (861 mg, 1.59 mmol, 79%) were isolated.

^{1}H-NMR (600 MHz, CDCl3): δ (ppm) = 8.92 (d, J = 8.2 Hz, 1 H), 8.70 (dd, J = 8.2, 1.4 Hz, 1 H), 8.31 (d, J = 1.4 Hz, 1 H), 8.20 (d, J = 7.6 Hz, 2 H), 8.14 (d, J = 7.6 Hz, 1 H), 7.93 (d, J = 2.0 Hz, 1 H), 7.83 (dd, J = 8.9, 2.0 Hz, 1 H), 7.75 (d, J = 8.3 Hz, 1 H), 7.70 (td, J = 7.6, 1.3 Hz, 1 H), 7.65 (d, J = 7.6 Hz, 1 H), 7.62 (dd, J = 8.2, 1.4 Hz, 2 H), 7.58 (t, J = 7.6 Hz, 1 H), 7.53 (t, J = 8.3 Hz, 1 H), 7.40-7.46 (m, 4 H), 7.39 (t, J = 7.6 Hz, 1 H), 7.32 (td, J = 8.3, 1.4 Hz, 2 H); ^{13}C-NMR (150 MHz, CDCl3): δ (ppm) = 179.2, 141.8, 141.3, 140.8, 139.4, 139.2, 136.9, 132.6, 132.2, 130.9, 130.0, 129.3, 128.0, 127.1, 126.8, 126.1, 126.0, 125.9, 125.1, 124.5, 123.6, 123.2, 123.1, 121.4, 120.8, 120.3, 119.8, 119.7, 111.0, 110.2,

109.7; APCI-MS (*m/z*): $[M+H]^+$ calcd. for $C_{37}H_{22}N_2OS$, 543.1526; found. 543.1525.

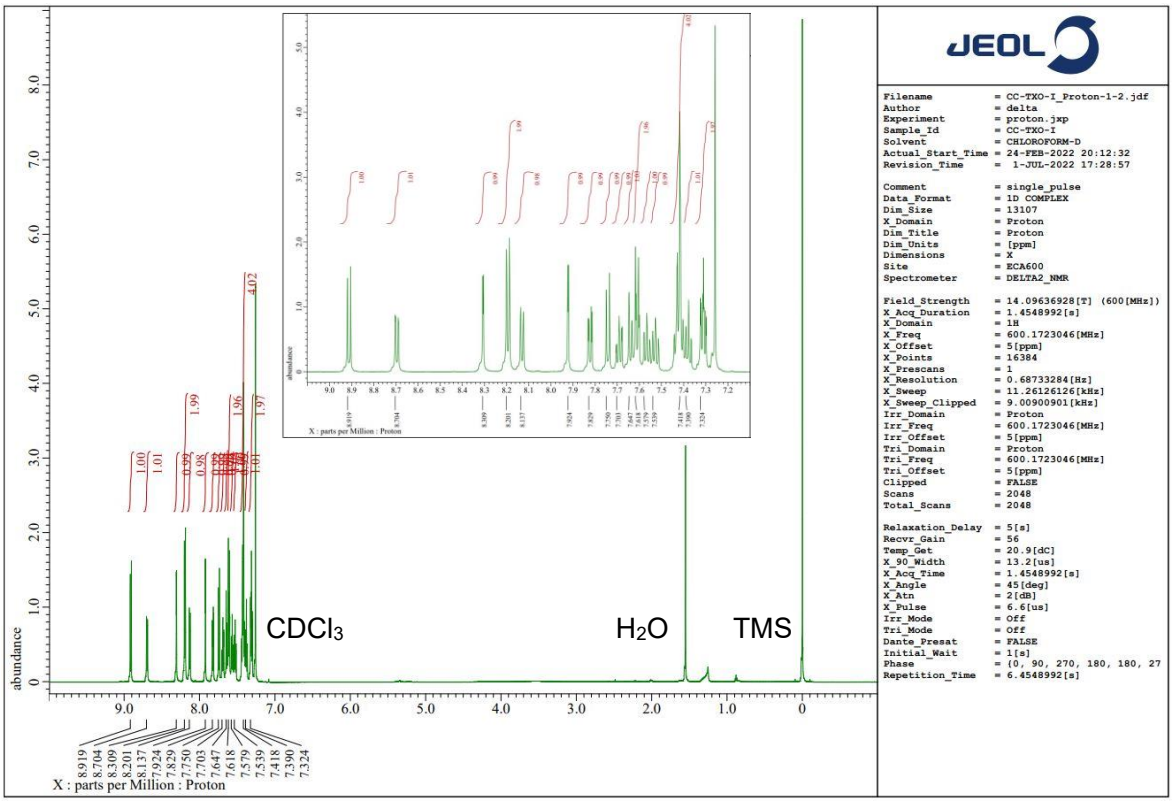

^{1}H NMR spectrum of CC-TXO-I after train sublimation.

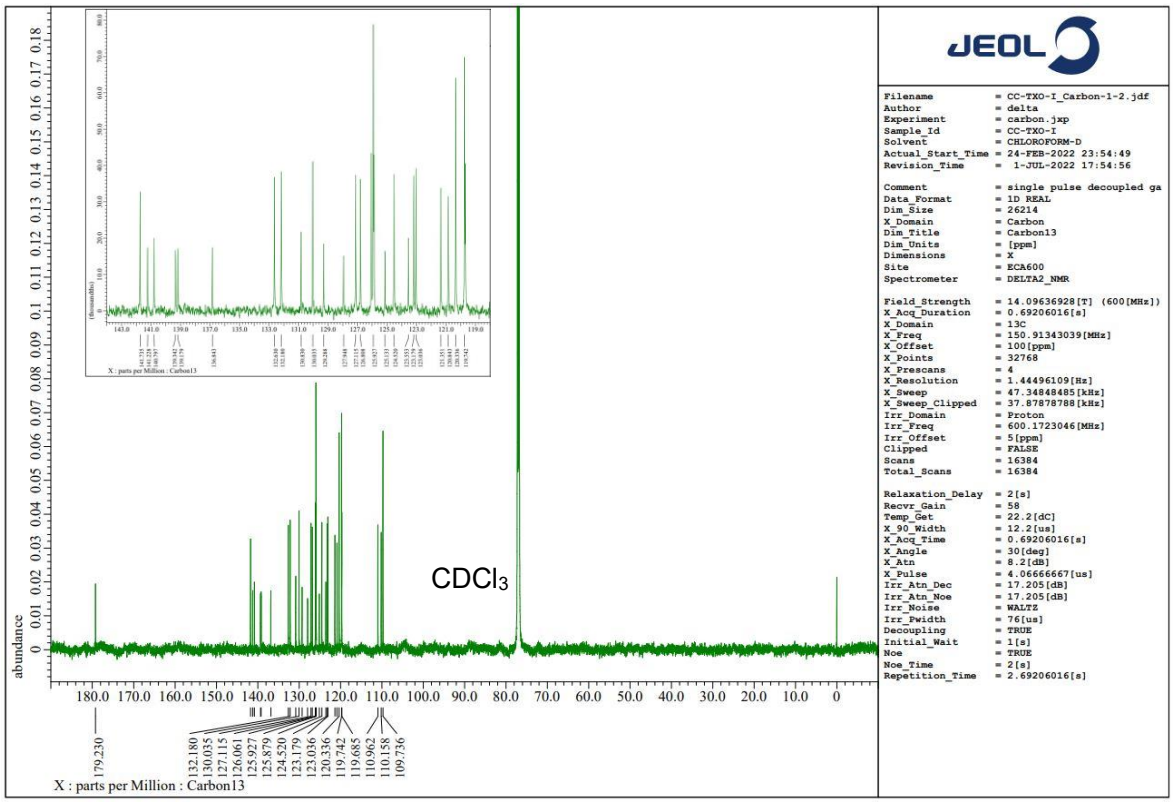

^{13}C NMR spectrum of CC-TXO-I after train sublimation.

1.3. Photophysical characterizations

The oxygen-free toluene solution of CC-TXO-I at a concentration of 1×10^{-4} M was prepared in a glove box (UniLab, MBraun, Germany). The concentrations of oxygen and water in the glove box were less than 0.1 ppm. To prepare solution-processed films, spin coating was conducted with solutions in 2.5 mg mL^{-1} with 1000 rpm for 30 seconds on fused quartz substrates, and the fabricated films were dried at 30 ℃ for 30 minutes under vacuum. Also, vacuum-processed films were deposited on fused quartz substrates with vacuum-deposition equipment (SE-4260, ALS Technology, Japan). The pressure in the chamber was ~10^{-5} Pa and the thickness of films were 50 nm.

For photophysical characterizations, a UV-vis spectrophotometer (UV-2600, SHIMADZU, Japan), a spectrofluorometer (FluoroMax Plus, HORIBA, Japan), and an absolute photoluminescence (PL) quantum yield (Φ_{PL}) spectrometer (C9920-02, Hamamatsu Photonics, Japan) were used. In addition, the transient PL decay curves were obtained by a fluorescence lifetime measurement system (Quantaurus-Tau C11367-01, Hamamatsu Photonics, Japan), and it was used in combination with a cryostat (Optistat DN2, Oxford Instruments, UK) for a temperature-dependent transient PL decay. Fig. S1 shows an example of a transient PL measurement for 6 vol% CC-TXO-I:PPF doped film.

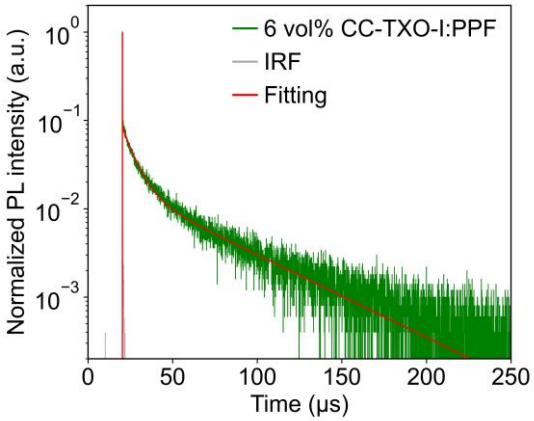

Fig. S1. Transient PL decay curve of 6 vol% CC-TXO-I:PPF doped film; experimental data (green line), fitting curve (red line), and instrument response function (gray line).

1.4. Fabrication of OLEDs

First, a patterned indium tin oxide (ITO) glass substrate was cleaned by UV-ozone treatment for 15 minutes. Then, each layer was deposited at the pressure of ~10^{-4} Pa with vacuum-deposition equipment (SE-4260, ALS Technology, Japan). After deposition of organic layers and an electrode, the device was sealed by a UV-curable resin in the glove box.

An OLED performance was characterized with a source meter (2400, Keithley, USA) and an EQE measurement system (C9920-12, Hamamatsu Photonics, Japan).

2. Supplementary figures and tables

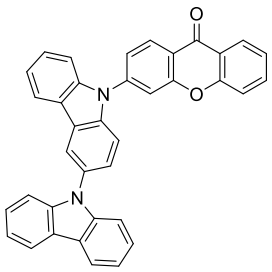

Fig. S2. Chemical structure of CCX-I.[4)]

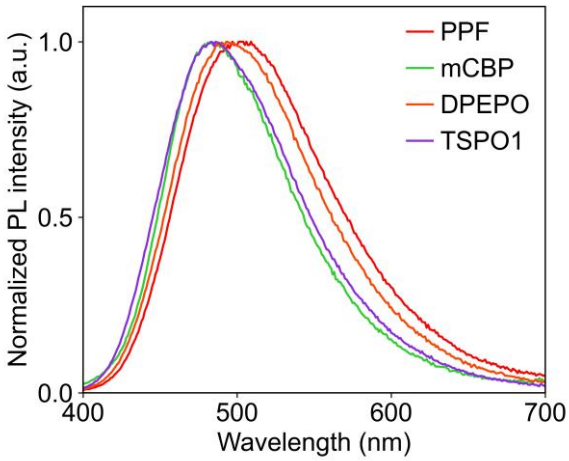

Fig. S3. PL spectra of solution-processed doped films of 6 wt% CC-TXO-I.

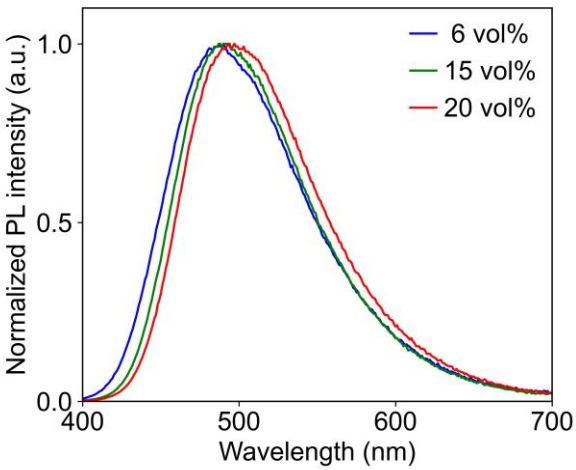

Fig. S4. PL spectra of vacuum-processed doped films of *X* vol% CC-TXO-I:PPF (*X* = 6, 15, 20).

Table SI. Photophysical properties of solution-processed doped films of 6 wt% CC-TXO-I.

Host	λ_{MAX}[a)] (nm)	Φ_{PL}[b)] (%)
PPF	506	68
mCBP	483	15
DPEPO	493	67
TSPO1	486	57

a) Emission peak maximum wavelength excited at 365 nm. b) Φ_{PL} excited at 365 nm.

Table SII. Photophysical properties of vacuum-processed doped films of *X* vol% CC-TXO-I:PPF.

X (vol%)	λ_{MAX}[a)] (nm)	Φ_{PL}[b)] (%)
6	486	84
15	488	83
20	493	84

a) Emission peak maximum wavelength excited at 365 nm. b) Φ_{PL} excited at 365 nm.

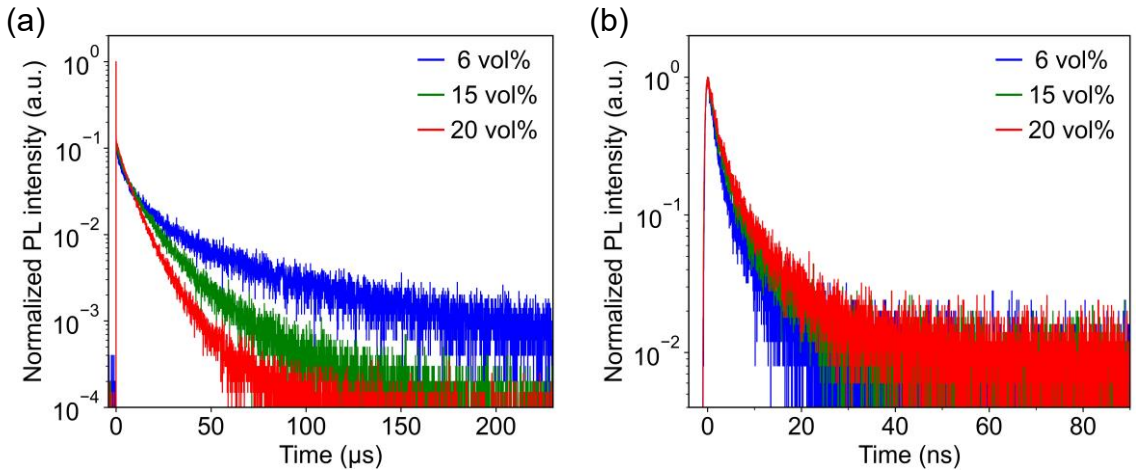

Fig. S5. Transient PL decay curves of vacuum-processed films of *X* vol% CC-TXO-I:PPF excited at 280 nm. (a) All region. (b) Prompt region.

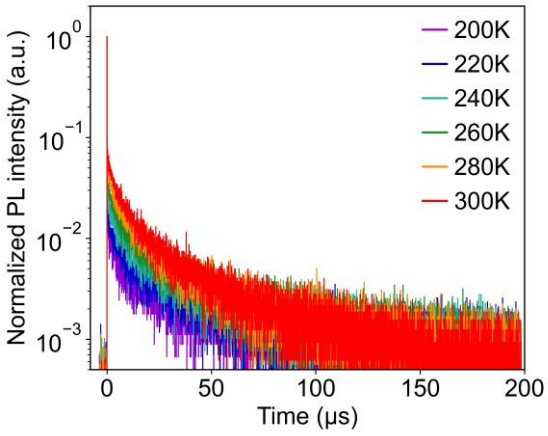

Fig. S6. Transient PL decay curves of 6 vol% CC-TXO-I:PPF vacuum-processed film measured at 200, 220, 240, 260, 280, and 300 K.

Table SIII. Photophysical properties of doped films of the reported TXO-based TADF emitters and performance of OLEDs using those doped films as EMLs.

Emitter	λ_{MAX}[a] (nm)	Φ_{PL} (%)	EQE_{max}[b] (%)	Reference
6 vol% CC-TXO-I:PPF	486	84	19.0	This work
10 wt% CzTXO:DPEPO	N.A.[c]	29.6	11.2	[5]
10 wt% DCz-TXO:DPEPO	N.A.[c]	34.8	11.5	[5]
3 wt% 3,6-2TPA-TX:CBP	N.A.[c]	35.0	23.7[d]	[6]
10 wt% 1,6-2TPA-TX:CBP	N.A.[c]	2.5	2.23	[6]
10 wt% MCz-TXT:mCBP	490	92	25.8	[7]
5 vol% MCz-TXO:CzSi	475	64.7	17.4	[8]
50 wt% Dye1:TFB	472	33	2.23	[9]
50 wt% Dye2:TFB	464	51	3.16	[9]

a) Emission peak maximum wavelength of a doped film. b) Maximum EQE of OLEDs based on the doped film. c) No data was provided. d) Judging from the Φ_{PL} value of 35.0%, the EQE_{max} is considered to be too high.

References

1) T. Kitawaki, Y. Hayashi, A. Ueno and N. Chida, Tetrahedron **62**, 6792 (2006).
2) M. B. Ponce, F. M. Cabrerizo, S. M. Bonesi and R. Erra-Balsells, Helv. Chim. Acta **89**, 1123 (2006).
3) H. Liu, G. Cheng, D. Hu, F. Shen, Y. Lv, G. Sun, B. Yang, P. Lu and Y. Ma, Adv. Funct. Mater. **22**, 2830 (2012).
4) T. Miwa, S. Kubo, K. Shizu, T. Komino, C. Adachi and H. Kaji, Sci. Rep. **7**, 284 (2017).
5) Z. Wang, Y. Li, X. Cai, D. Chen, G. Xie, K. K. Liu, Y. C. Wu, C. C. Lo, A. Lien, Y. Cao and S. J. Su, ACS Appl. Mater. Interfaces **8**, 8627 (2016).
6) Y. Li, X. L. Li, D. Chen, X. Cai, G. Xie, Z. He, Y. C. Wu, A. Lien, Y. Cao and S. J. Su, Adv. Funct. Mater. **26**, 6904 (2016).
7) N. Aizawa, A. Matsumoto and T. Yasuda, Sci. Adv. **7**, eabe5769 (2021).
8) Y. Ren, Y. Wada, K. Suzuki, Y. Kusakabe, J. Geldsetzer and H. Kaji, Appl. Phys. Express **14**, 071003 (2021).
9) S. Nasiri, M. Hosseinnezhad, M. Rabiei, A. Palevicius, Z. Rahimi, G. Janusas and A. Vilkauskas, Opt. Mater. **127**, 112320 (2022).